Journal of Materials Chemistry C



PAPER

View Article Online
View Journal | View Issue



Cite this: *J. Mater. Chem. C,* 2017, **5**, 5757

ultrafast plasmonic relaxation in conducting metal oxide nanocrystals†

Robert W. Johns,‡^{ab} Michelle A. Blemker,‡^c Michael S. Azzaro,^c Sungyeon Heo,^b Evan L. Runnerstrom,^{bd} Delia J. Milliron^b and Sean T. Roberts*^c

Charge carrier concentration dependence of

Electronically doped metal oxide nanocrystals exhibit tunable infrared localized surface plasmon resonances (LSPRs). Despite the many benefits of IR resonant LSPRs in solution processable nanocrystals, the ways in which the electronic structure of the host semiconductor material impact metal oxide LSPRs are still being investigated. Semiconductors provide an alternative dielectric environment than metallically bonded solids, such as noble metals, which can impact how these materials undergo electronic relaxation following photoexcitation. Understanding these differences is key to developing applications that take advantage of the unique optical and electronic properties offered by plasmonic metal oxide NCs. Here, we use the two-temperature model in conjunction with femtosecond transient absorption experiments to describe how the internal temperature of two representative metal oxide nanocrystal systems, cubic WO_{3-x} and bixbyite Sn-doped In₂O₃, change following LSPR excitation. We find that the low free carrier concentrations of metal oxide NCs lead to less efficient heat generation as compared to metallic nanocrystals such as Ag. This suggests that metal oxide NCs may be ideal for applications wherein untoward heat generation may disrupt the application's overall performance, such as solar energy conversion and photonic gating.

Received 7th February 2017, Accepted 9th March 2017

DOI: 10.1039/c7tc00600d

rsc.li/materials-c

1. Introduction

Nanocrystals (NCs) with sufficiently high concentrations of charge carriers exhibit the metallic property of a localized surface plasmon resonance (LSPR). This optical phenomenon, which entails the dipolar excitation of all free charge carriers in the NC into a collective oscillation, has a large extinction cross section and is commonly employed to concentrate light into nanoscopic volumes. Common goals for exploiting this intense concentration of energy are to use it to sensitize other optical transitions, produce hot carriers for charge transfer reactions, or to locally generate heat. ^{1–3} In the case of colloids made from NCs that are substantially smaller than the central resonance wavelength (with diameter $<\lambda_{\rm LSPR}/20$) heat generation is the dominant

relaxation mechanism following excitation.4 These smaller

Heat generation as a pathway for plasmonic decay is well-studied in metallic thin film and nanoparticle systems, *i.e.* Au and Ag.^{10–12} Only recently, however, have scientists started to investigate LSPR energetic relaxation in semiconductor-based plasmonic materials.^{13–18} Electronically doped semiconductors, such as metal oxides and metal chalcogenides, exhibit LSPRs at near infrared (NIR) and mid infrared (mid-IR) frequencies upon introduction of aliovalent dopants or other charge donating defects such as vacancies. These systems have generated a great deal of interest because their LSPR is controlled *via* charge carrier concentration, rather than by changing NC physical dimensions (and thus, ensuring colloidal materials processing

NCs, unlike larger NCs, do not scatter light back to the far field as a relaxation pathway. Instead, the energy of the excited LSPR results in thermalized electrons near the Fermi level whose energy is subsequently converted to phonons within the lattice *via* scattering, and eventually dissipated to the environment as heat. In some NC systems, this heat generation is so effective that plasmonic NCs have been used for photothermal therapy, photoacoustic imaging, catalysis, and even local steam generation. ^{5–8} Understanding LSPR-based heating in NC systems is important not only for the applications listed above, but also for efficiency and stability concerns in NC LSPR device applications where heat generation may be detrimental to performance. ⁹

^a Department of Chemistry, University of California, Berkeley, Berkeley, California 94720, USA

^b McKetta Department of Chemical Engineering, The University of Texas at Austin, 200 East Dean Keeton Street, Austin, Texas 78712, USA

^c Department of Chemistry, The University of Texas at Austin, Austin, Texas 78712-1224, USA. E-mail: roberts@cm.utexas.edu

^d Department of Materials Science and Engineering, The University of California, Berkeley, Berkeley, California 94720, USA

[†] Electronic supplementary information (ESI) available. See DOI: 10.1039/

[‡] These two authors contributed equally to this manuscript.

and handling). 19-24,33 In plasmonic systems, the plasma frequency $(\omega_{\rm p})$, the electronic damping constant (Γ) , and high frequency dielectric constant (ε_{∞}) are the primary material constants that dictate the LSPR properties, which can be modeled using the Drude dielectric function $(\varepsilon_p(\omega))$ when the LSPR has little to no energetic overlap with other electronic transitions,

$$\varepsilon_{\rm p}(\omega) = \varepsilon_{\infty} - \frac{\omega_{\rm p}^2}{\omega^2 + i\omega\Gamma}$$
 (1)

Importantly in n-type systems, ω_p depends on both the free electron concentration of the material (n_e) and the dispersion of the conduction band *via* the free carrier effective mass (m). ω_p is then calculated using the fundamental electron charge (e) and the permittivity of free space (ε_0) ,

$$\omega_{\rm p} = \sqrt{\frac{n_{\rm e}e^2}{\varepsilon_0 m}} \tag{2}$$

As n_e changes with doping, so does the plasma frequency. These doped semiconductor NCs can thus maintain a fixed geometry and be tuned to exhibit LSPR over a wide range of frequencies in the infrared (IR) depending on the desired application.

With regards to heat production, the IR LSPRs in metal oxide systems should lead to less heat generation per absorbed photon as compared to the higher energy visible LSPRs in metal systems, based on the energy of photons they absorb. Additionally, to determine the amount of heat generated by each material for a specified photon flux, one must consider how both optical density is affected by the dielectric function and how a material's electronic structure and physical constants impact heat generation. For example, LSPR absorbance can be calculated from the dielectric function using Mie theory from the relationship of optical absorbance to volume of the NC (V), the wavevector (k), and the dielectric constant of the medium within which the NC resides $(\varepsilon_{\rm m})$,

$$\sigma_{abs} = 3Vk\sqrt{\varepsilon_{m}}\operatorname{Imag}\left\{\frac{\varepsilon_{p} - \varepsilon_{m}}{\varepsilon_{p} + 2\varepsilon_{m}}\right\}$$
(3)

As the imaginary component of the dielectric function increases with the square of the plasma frequency, the absorbance cross section of an LSPR increases linearly with $n_{\rm e}$,

$$\varepsilon_{\text{p,imag}} = \frac{\omega_{\text{p}}^2 \Gamma}{\omega(\omega^2 + \Gamma^2)} \tag{4}$$

Hence, not only does an LSPR absorb higher energy photons as carrier concentration increases, but it also absorbs them with higher efficiency per volume of NCs. Or put another way, the ratio of total light energy absorbed by the LSPR of a NC (which is based on electrons) to the total phonon bath the NC provides (which is based on volume of material) decreases at lower carrier concentrations. As a result, for a higher frequency LSPR there is a relatively smaller phonon bath available to dissipate energy. This suggests that among two NC samples with equal optical densities, metal NCs should heat up more than metal oxide NCs for the same total absorbed energy flux, as it is being converted to heat in a smaller total volume of NCs.

In this study, we applied the two-temperature model (TTM) along with our material-dependent optical densities (calculated with Drude dielectric functions) to better understand the expected dependence of carrier concentration on heat generation from LSPR absorbance.²⁵ We compared the behavior of two doped metal oxide systems, cubic WO_{3-r} and bixbyite Sn:In₂O₃, to those of Ag NCs. Each material's dielectric functions and other necessary material parameters were ascertained by utilizing assumptions of the free electron approximation. We performed ultrafast pumpprobe transient absorption measurements on colloids of WO_{3-x} and Sn:In₂O₃ NCs to validate that the TTM is applicable to these systems and to determine the electron-phonon coupling constants for each. We found that the maximum lattice temperature reached in colloidal Ag NCs is substantially higher than that of metal oxide NCs of the same size prepared at similar optical density and excited under identical input power. This result indicates that as carrier concentration is reduced, the generation of lattice heat decreases following LSPR absorption.

Experimental

2.1 Sample preparation of $Sn:In_2O_3$ and WO_{3-x} colloids

NCs of WO_{3-x} and Sn:In₂O₃ (5 atom% of Sn) of radius 3 nm and 6.5 nm, (ESI,† Fig. S1) respectively, were synthesized following established literature procedures. 26,27 NC dispersions were prepared of each sample in hexane and tetrachloroethylene (TCE), which were optically characterized in NIR quartz 1 mm path length cuvettes on an Agilent Cary 5000 UV-vis-NIR spectrophotometer.

2.2 Transient absorption measurements

Transient absorption (TA) measurements were conducted using a 13.5 W amplified Ti:sapphire laser operating at 3 kHz with a center wavelength of 804 nm and a pulse length of ~ 90 fs (Coherent Legend Elite Duo). The Ti:sapphire output was split, and part of the 804 nm output was used to directly excite WO3-x samples. Excitation pulses for Sn:In2O3 samples were generated by down-converting a portion of the Ti:sapphire output to 1800 nm using an optical parametric amplifier (Light Conversion TOPAS-Prime). Probe pulses for both sets of experiments were created by splitting off a small portion of the 1800 nm line and focusing it into a 6 mm thick undoped Yittrium Aluminum Garnet (YAG) crystal to create a supercontinuum with bandwidth spanning from 550 nm to >1700 nm. Probe light was spectrally dispersed using a 500 mm Czerny-Turner spectrometer (Acton Instruments SpectraPro 2556) and two detectors were used for data collection, a CCD camera for visible wavelengths (Princeton Instruments PyLoN 100-BR), and a 512-pixel InGaAs linear imaging sensor (Hamamatsu G11620-512DA) for infrared wavelengths. WO_{3-x} and Sn:In2O3 dispersions were stirred thoroughly throughout measurements. The optical densities at λ_{LSPR} were 0.17 and 0.22 for these samples, respectively. A cross-correlation between the pump and supercontinuum probe pulses measured using sample cuvettes that had been filled with neat solvent was found to have a FWHM of 130 fs.

3. Results and discussion

3.1 Optical characterization of NC LSPRs

In order to model heat generation in our NCs, the dielectric function must be properly identified so that quantitative analysis can be performed. This is achieved by fitting the absorption spectra of samples using the Beer-Lambert law, $A_{\text{mie}} = N\sigma_{\text{abs}}L/\ln(10)$.²⁸ Here, N is the particle number density $N = 3f_v/4\pi R^3$, with f_v representing the NC volume fraction and R the NC radius, L the cuvette pathlength and σ_{abs} the absorption cross section (eqn (3)). Using literature values for the high frequency dielectric constants of our materials (ε_{∞} = 6 for WO_{3-x} and 4 for Sn:In₂O₃), ^{29,30} the volume fraction (f_v) , plasma frequency (ω_p) , and damping constant (Γ) can be determined for each sample from least squares fits to their steady-state absorption spectrum (Fig. 1A and Fig. S2, ESI†). The results of this fitting routine and other relevant constants for our optical simulations are tabulated below (Table 1). These dielectric functions, as well as one formed for Ag from literature values, were used to simulate absorption spectra for the three materials (Fig. 1B and C). 31,32

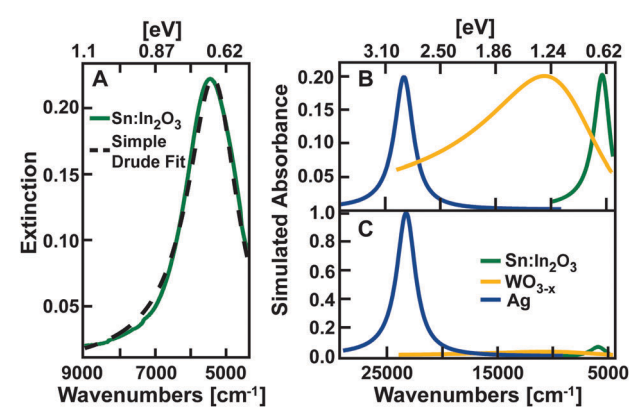


Fig. 1 (A) Experimental extinction spectrum of Sn:In₂O₃ NCs dispersed in TCE and the simple Drude fit used to extract optical constants. (B) Ag (blue), WO_{3-x} (yellow), and Sn:In₂O₃ (green) simulated absorption spectra from samples at different $f_{\rm v}$ to obtain a 0.2 OD at $\lambda_{\rm LSPR}$. (C) Ag, WO_{3-x}, and Sn:In₂O₃ simulated absorption spectra for identical NC volume fractions of 1.3×10^{-4} .

Table 1 Dielectric constant parameters

	ϵ_{∞}	$\omega_{\rm p}~({\rm cm}^{-1})$	Γ (cm ⁻¹)	$f_{ m v}$	$n_{\rm e}~({\rm cm}^{-3})$	$m/m_{\rm e}$
Ag			2054		$5.84 \times 10^{22 d}$	
WO_{3-x}	6^b	33 120	12540	6.80×10^{-3}	1.71×10^{22}	1.4^e
Sn:In ₂ O ₃	4^c	14 978	1727	4.50×10^{-4}	8.75×10^{20}	0.35^{c}

^a Ref. 31. ^b Ref. 29. ^c Ref. 30. ^d Ref 32. ^e Ref. 34.

In Fig. 1B, all three samples were modeled with different values of $f_{\rm v}$ in order to reach an optical density (OD) of 0.2 at $\lambda_{\rm LSPR}$ (as tabulated in Table 2). A volume fraction more than $10\times$ larger was necessary to reach the same OD for Sn:In₂O₃ as Ag because of their difference in $\omega_{\rm p}$ as illustrated in eqn (3) and (4).

This effect is displayed even more clearly when all three samples are plotted at the same f_v (Fig. 1C). One can see that materials with higher carrier concentrations absorb substantially more light. Additionally, LSPR damping further modifies the relative OD of an equal concentration of NC samples as the peak amplitude of a LSPR will decrease as its damping (and hence linewidth) increases. For this reason our WO_{3-x} sample has an even lower OD at its λ_{LSPR} than would be expected from its higher n_e than Sn:In₂O₃ as illustrated in the fixed volume fraction spectra. On a practical note, directly comparing LSPR damping from visible frequencies to NIR frequencies is best done in energy units as the non-linear relationship of wavelength to energy both broadens and distorts LSPR peak shapes in the IR. In applications where it is standard to prepare a sample with a fixed optical density, researchers are examining NC suspensions with drastically different concentrations between material classes. The implications of this with regards to the amount of heat generated locally about each NC following LSPR excitation are severe, as we illustrate below.

3.2 Two-temperature model predictions of LSPR heating in metal oxides

The most common approach for understanding how LSPR energy is converted into lattice heat is the TTM. Though forms of this model exist that can account for the rise in electron temperature ($T_{\rm e}$) as the LSPR thermalizes or on much longer timescales as energy leaves the phonons of the NC and diffuses into the vibrational bath of the solvent, here we are only concerned with the short timescale evolution of $T_{\rm e}$ into lattice temperature ($T_{\rm L}$).¹³ A pair of coupled differential equations is used that incorporate the electron heat capacity $\gamma T_{\rm e}$ and the material specific heat $C_{\rm p}$.²⁵

$$\gamma T_{\rm e} \frac{\mathrm{d}T_{\rm e}}{\mathrm{d}t} = -G(T_{\rm e} - T_{\rm L}) \tag{5a}$$

$$C_{\rm p} \frac{\mathrm{d}T_{\rm L}}{\mathrm{d}t} = G(T_{\rm e} - T_{\rm L}) \tag{5b}$$

Here, we assume that through the electron–phonon coupling constant (G) one can track how energy is transferred to the lattice from hot electrons until the two temperatures equilibrate. By calculating the initial electron temperature $(T_{\rm e,i})$ and lattice temperature $(T_{\rm L,i})$, taken to be room temperature at $T=298{\rm K})$ we

Table 2 Two temperature model constants

	γ (J K ⁻² cm ⁻³)	$C_{\rm p} ({\rm J~K^{-1}~cm^{-3}})$	$G (J K^{-1} s^{-1} cm^{-3})$	$f_{ m v}$ (0.2 OD)	OD $(1.3 \times 10^{-4} f_{v})$
Ag	$6.51 \times 10^{-5 a}$	2.47^{b}	3.10×10^{10b}	2.6×10^{-5}	1.0
WO_{3-x}	5.50×10^{-5}	3.03 ^c	9.64×10^{10}	8.6×10^{-4}	3.04×10^{-2}
$Sn:In_2O_3$	5.11×10^{-6}	1.1418^d	1.25×10^{10}	3.7×10^{-4}	7.14×10^{-2}

^a Ref. 32. ^b Ref. 35. ^c Ref. 36. ^d Ref. 37.

can track the temperature progression of both excited NC electrons and phonons over time. As G is not a constant easily found for conducting metal oxides, one can arrive at this constant using transient absorption measurements where the pump fluence is kept at sufficiently low flux such that T_L is not considerably raised above room temperature^{34,35} (see ESI,† Fig. S3 and S4 for additional details). $T_{e,i}$ can be calculated using the pump fluence (F), the fraction of incident photons absorbed by the sample at the pump wavelength (A(F)), γT_e at room temperature, and the optical path length (L).

$$T_{\rm e,i} = \frac{FA(F)}{L\gamma T_{\rm e} f_{\rm v}} \tag{6}$$

Though γT_e is a known value for most metals, calculating it for metal oxides at a particular dopant concentration requires consideration of how the electronic structure of a material impacts its thermalized electrons. Regardless of how many electrons occupy the conduction band of a metal, the thermal energy is only stored within the electrons that occupy states within a few k_bT of the Fermi level. How many electrons participate in sharing the thermal energy is determined by the local density of states at the Fermi level as well as the amount of energy stored in the electrons. The electron heat capacity (C_e) is expressed as γT_e where γ is calculated from the local density of states at the Fermi level ($g(\varepsilon_f)$):

$$C_{\rm e} = \gamma T_{\rm e} = \frac{\pi^2 k_{\rm b}^2}{3} g(\varepsilon_{\rm f}) T_{\rm e} \tag{7}$$

In the free electron approximation, the local density of states is expressed as a function of the Fermi wavevector (k_f) :

$$g(\varepsilon_{\rm f}) = \frac{m_{\rm e}k_{\rm f}}{\pi^2\hbar^2} \propto m_{\rm e}n_{\rm e}^{\frac{1}{3}} \tag{8}$$

where $m_{\rm e}$ refers to the free electron mass. While this alone can be used to scale γ for one free electron gas of a given n_e to another, in hopes of also accounting for real material properties one should also consider the definition of the electron effective mass, which accounts for the dispersion of the conduction band. Depending on this dispersion, the expected free electron $\gamma_{\rm FE}$ can over or underestimate the materials' real electronic heat capacity γ_{real} . The effective mass is used to correct for this deviation from the free electron gas approximation.

$$\frac{m}{m_{\rm e}} = \frac{\gamma_{\rm real}}{\gamma_{\rm FE}} \tag{9}$$

Examining these equations, it is apparent that one can scale the electron heat capacity to account for the local density of states for a real material based on both its carrier concentration and its electron effective mass. This allows for the known γ of metals to be used to calculate those of the doped semiconductors.

$$\frac{\gamma_{\text{real},1}}{\gamma_{\text{real},2}} = \frac{m_1 n_{\text{e},1}^{\frac{1}{3}}}{m_2 n_{\text{e},2}^{\frac{1}{3}}}$$
(10)

Using this relationship to determine an unknown γ ($\gamma_{\text{real},1}$) from a known material's γ ($\gamma_{real,2}$) is quite simple by using the electron concentration as extracted from the Drude fit and the material's electron effective mass.

With these calculated electron heat capacities, we simulated the two-temperature response of our three materials on a single absorbed photon per NC basis as well as under experimental conditions for NC dispersions like those illustrated in Fig. 1. The relevant constants used for these equations are assembled in Table 2. For the single photon case, we sought to understand what the expected effect of carrier concentration has on the heat generation properties of a material (Fig. 2). In Fig. 2A, for each of our test materials we used the values of γ to calculate C_e at room temperature, C_p , and G given in Table 2 to show what the expected initial electron temperature would be for a particle with R = 7 nm following the absorption of the energy from a single photon at its λ_{LSPR} . Sn:In₂O₃, which has a very low value of γ due to its low n_e and m/m_e , reaches a high initial $T_{e,i}$ even with its low LSPR energy. In contrast, Ag and WO_{3-x} reach lower $T_{e,i}$ due to their larger γ values, with Ag being hotter than WO_{3-x} as a result of its higher energy LSPR. Following photon absorption, all three materials cool to a value of T_L that is nearly equal to room temperature, as a single photon imparts only a marginal amount of energy to each NC relative to the amount needed to heat it substantially, which is determined by the material's bulk heat capacity, $C_{\rm p}$.

One of the important properties of doped semiconductors is their tunable LSPR frequencies. The free electron concentration of Sn:In2O3 is increased via doping. Fig. 2B plots the expected relationship of initial electron temperature, $T_{e,i}$, as n_e is varied over a range that tunes λ_{LSPR} from the mid-IR to the near-IR spectral range. Both λ_{LSPR} and γ depend on n_e and increase with higher carrier densities, leading to an overall increase in the expected Te,i following LSPR excitation for higher dopant concentrations. Importantly, since ω_p increases with the square root of n_e (eqn (2)) while γ increases as the cube root, there is a positive trend in single-photon $T_{e,i}$ with n_e .

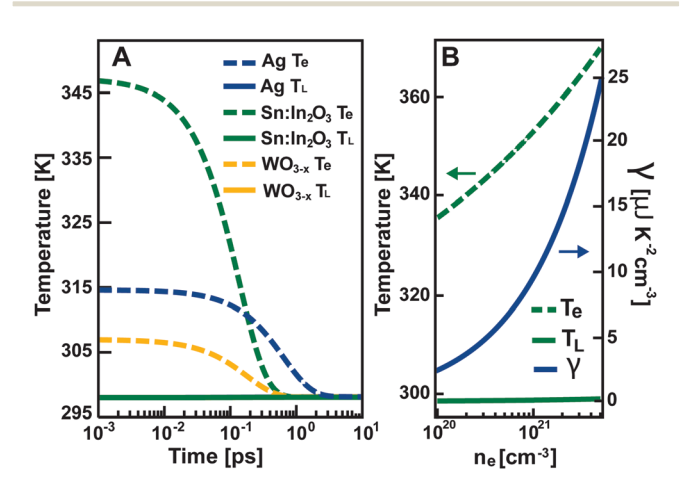


Fig. 2 (A) Calculated electron and phonon temperatures following single photon excitation at each NC's LSPR frequency. Initial system temperatures for calculations were 298 K. (B) (green dashed) Initial electron temperature with respect to carrier concentration, $n_{\rm e}$, for single-photon excitation at $\lambda_{LSPR}(n_e)$. (blue) Change in electronic heat capacity with increasing carrier concentration. (green solid) The resulting lattice temperature as the λ_{LSPR} is increased

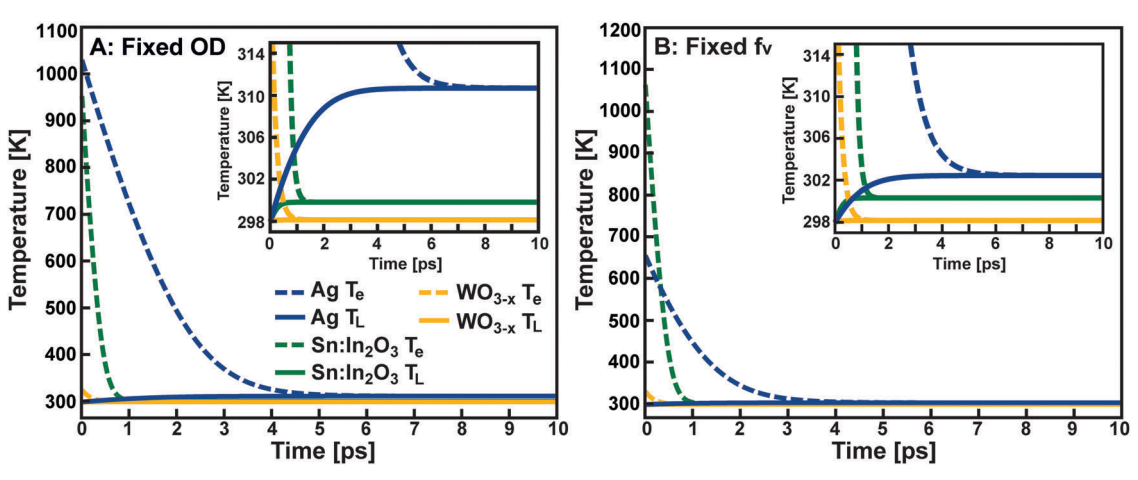


Fig. 3 (A) TTM calculations for 14 nm diameter Ag, WO $_{3-x}$, and Sn:In $_2$ O $_3$ NCs with an 0.2 OD absorbance at the LSPR frequency and an incident pump fluence of 100 μ J cm $^{-2}$ starting from 298 K. Inset with different temperature range scale demonstrates the lattice temperature change. (B) TTM calculations for the same Ag, WO $_{3-x}$, and Sn:In $_2$ O $_3$ NCs with a consistent volume fraction of 1.3×10^{-4} . Inset with different temperature range scale demonstrates the lattice temperature change.

We also investigated the colloid behavior at a fixed fluence of 100 μ J cm⁻² for our series of materials for both fixed OD and fixed $f_{\rm v}$ as seen in Fig. 1 to understand what temperatures are being reached upon pumping the LSPR (Fig. 3). In the case of a fixed OD of 0.2 (Fig. 3A), the volume fraction of Ag is much smaller than for the metal oxides. As a result, $T_{\rm e,i}$ follows the trend of γ as the same total energy absorbed in each sample will lead to larger initial temperatures in materials with smaller heat capacities. However, as this energy is converted to $T_{\rm L}$, Ag ends up much hotter than the metal oxides since the energy is shared between a smaller volume of NCs. The resulting $T_{\rm L}$ of 310 K in Ag, when compared to 298 K in WO_{3-x} and 300 K in Sn:In₂O₃, demonstrates how the larger $f_{\rm v}$ of the metal oxides needed to reach OD 0.2 partitions the energy among a larger amount of solid.

Though it shouldn't be surprising that the metal nanoparticle lattice was heated considerably given prior experimental demonstrations of noble metal LSPR heating, the metal oxides display qualitatively different behavior and are hardly heated by photoexcitation. In fact, in WO_{3-x} the ratio of γ to C_p is so small that it is warmed less than 1 K. Though there is less material of WO_{3-x} than $Sn:In_2O_3$, suggesting it would get warmer given similar energy stored in the electrons, its large phonon density of states (resulting in its substantially larger C_p than $Sn:In_2O_3$ or Ag) makes WO_{3-x} all but immune to LSPR based heating.

When considering the fixed f_v case (Fig. 3B) where the same fluence is radiated upon the same amount of material, the metal oxides still reach a lower final $T_{\rm L}$ than Ag because they absorb significantly less light than Ag for the same amount of material. Sn:In₂O₃ again exhibits exceptionally high $T_{\rm e}$, due to its low γ , much like in the single photon case. Unlike the fixed OD case, there is now the same relative amount of each material present so the $T_{\rm L}$ reached is strongly dominated by $C_{\rm p}$. The redistribution of energy to reach equilibrium in the system causes an increase in $T_{\rm L}$, which is dependent on the amount of energy stored in the electrons (based on $T_{\rm e,i}$ and γ), and what temperature change that amount of energy would

induce in the lattice, given the material's C_p . Here, more energy is stored in the lattice than in the electrons at the same T. Our simulations illustrate that metal oxides, generally, should not substantially heat via their LSPR due to their low γ to C_p ratio on a per volume of material basis. Since most transient optical experiments are made with samples chosen to have ODs in the range of 0.1–0.4 to ensure high signal-to-noise ratio data collection, in general metallic samples will always reach a higher T_L since less material is present. In order to differentiate the ability of a material to produce heat versus how much heat is being made at a given colloid concentration, careful consideration should be made for accounting for the carrier concentration dependence of a sample's OD.

3.3 Transient optical spectra of metal oxide LSPRs

To determine the G values needed for our modeling of LSPR relaxation in WO_{3-x} and Sn:In₂O₃ using the TTM, we performed transient absorption spectroscopy (TA) over a series of pump powers for both doped metal oxide NC colloids and then analyzed this data using established literature protocols. ³⁵ Briefly, G is extracted by measuring how the electronic decay rate of each NC sample changes with excitation density (Fig. S4, ESI†). This data is then extrapolated to zero input power, yielding the electron–phonon equilibration rate at the temperature of the NC's surroundings, τ_0 . Examining eqn (5a) above, we can relate this rate to G via the following relationship:

$$\tau_0 = \frac{\gamma T_0}{G} \tag{11}$$

where T_0 is temperature of the NC's surroundings (here taken to be 298 K). For additional details related to the determination of G, we direct interested readers to the ESI.†

Fig. 4 displays TA spectra of WO_{3-x} and $Sn:In_2O_3$ NCs. As is typically observed following LSPR excitation in metals, TA spectra of both metal oxide samples display a strong transient bleach on the blue side of the peak upon photoexcitation. ^{12,35} Over the first picosecond, this photobleaching signal undergoes a decay to

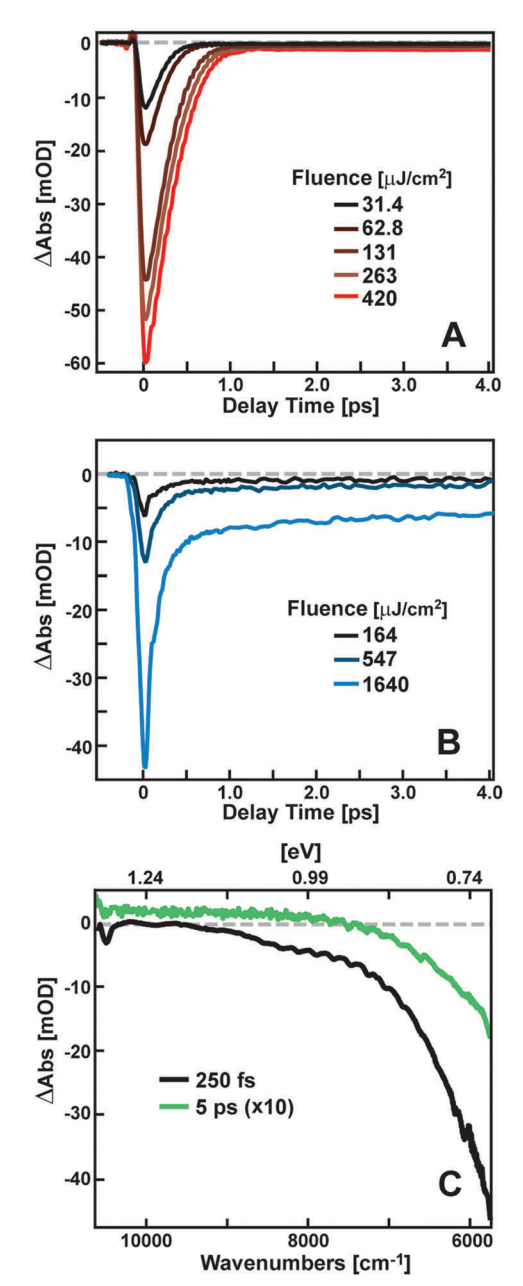


Fig. 4 (A) Transient kinetic trace of 14 nm diameter $Sn:In_2O_3$ NCs at ω_{probe} = $6061\,\mbox{cm}^{-1}$ (1650 nm) and varying incident pump powers. (B) Transient kinetic trace of 6 nm diameter WO_{3-x} NCs at ω_{probe} = 12 500 cm $^{-1}$ (800 nm) and varying incident pump powers. (C) Transient absorption spectra at 250 fs and 5 ps of Sn:In₂O₃ NCs.

a small offset that persists over at least a few nanoseconds (Fig. 4A and B, see Fig. S5 (ESI†) for longer timescale data). These short and long decay kinetics are consistent with two temperature relaxation as equilibration between hot electrons and the lattice is expected to occur over femtosecond to picosecond timescales, followed by lattice equilibration with its surroundings over much longer timescales.

To more rigorously ascribe these dynamics to changes in $T_{\rm e}$ and $T_{\rm L}$ for NC systems, transient spectra were examined for characteristic signatures of changes to the dielectric function resulting from thermally excited electrons and phonons

(as illustrated in Fig. S6, ESI \dagger). A change in $T_{\rm e}$ is expected to impact the dielectric function through a change in either ε_{∞} or $\omega_{\rm p}$, both of which cause a shift of the LSPR to lower energy. ^{15,38} This will produce a negative TA feature in the spectral range measured (on the higher energy side of the LSPR) that decays to zero approaching the tails of the peak, which is clearly in the early time transient spectrum of Sn:In2O3 measured at 250 fs in Fig. 4C. Over several ps (depending on G), hot electrons will eventually equilibrate with T_L . As T_L increases, the increased population of phonons decreases the electron-phonon scattering lifetime, resulting in an increase in LSPR damping. This increase in Γ manifests itself in LSPR absorption lineshapes as peak broadening, which generates a transient spectrum that is negative where the LSPR is centered which then goes through a zero-crossing near the peak's inflection point and displays a positive signal on either side of the LSPR. We can see in our spectra after a delay time of several ps, the transient signal resembles this expected lineshape (5 ps transient spectrum shown in Fig. 4C).

Characterizing full transient spectral responses can be challenging in metal oxide systems, as NIR LSPRs can make detector choice challenging, or, in the case of exceptionally broad peaks like those of WO_{3-x} , the non-linear relationship of energy to wavelength distorts the peak over large wavelength ranges. However, our single wavelength dynamics clearly display the expected LSPR TA response. In our power series data for both samples, with increasing power there was an increase in the strong initial transient bleach, which is consistent with reaching a higher $T_{\rm e,i}$. This increase in power also led to an increase in the intensity of the long-lived bleach that comes from reaching a higher equilibrated $T_{\rm L}$ following our TTM predictions. This enabled us to assume energy decay from both metal oxide LSPR materials progresses primarily through a two-temperature response, and instilled confidence in our extracted G values used for our estimations of heat generation in our systems.

4. Conclusions

As new varieties of doped semiconductor NCs exhibiting LSPR are synthesized and characterized, it is important to account for the differences in their optical properties during experiment design. Here, we have shown that two popular doped metal oxide materials are far less susceptible to LSPR-induced lattice heating than noble metals as a result of their lower n_e , material specific electronic structure, and thermal properties. Conversely, due to the exceptionally low effective mass of electrons in the conduction band of Sn:In₂O₃, we have shown that metal oxides can generate hotter electrons than metals depending on their electronic structure. Arriving at these results required consideration of how the optical density of an LSPR changes as a function of carrier concentration. Though these materials generate lattice heat less efficiently than metals, certainly on a per material basis they generate more heat than one would assume from fixed optical density studies. Metal oxides will consistently generate less lattice heat than metals due the lower energy photons they absorb in conjunction with their lower optical densities. When heating is desired, noble metals should regularly outperform most metal oxides, but in applications where heating may undesirably impact plasmonic applications, metal oxides could be a beneficial choice. The tunability of their high electron temperature, which LSPR frequency they absorb light at, and their ability to tune resonance frequencies while still forming stable colloids are all strong advantages of doped semiconductor NCs.

Acknowledgements

This work was supported by the Air Force Office of Scientific Research (S. T. R. Grant FA9550-15-1-0344), the National Science Foundation (S. T. R. Grant CHE-1610412 & D. J. M. Grant CHE-1609656), and the Robert A. Welch Foundation (D. J. M. Grant F-1848). M. A. B. would like to acknowledge support from a Provost Excellence Fellowship from the University of Texas at Austin, while R. W. J. acknowledges support from the Advanced Light Source doctoral fellowship provided by the Lawrence Berkeley National Laboratory. R. W. J. would also like to acknowledge Prof. Stephan Link for useful discussions related to optical modeling of LSPR in noble metals.

References

- 1 A. Furube, T. Yoshinaga, M. Kanehara, M. Eguchi and T. Teranishi, Angew. Chem., Int. Ed., 2012, 51, 2640-2642.
- 2 A. Furube, L. Du, K. Hara, R. Katoh and M. Tachiya, J. Am. Chem. Soc., 2007, 129, 14852-14853.
- 3 P. K. Jain, X. Huang, I. H. El-Sayed and M. A. El-Sayed, Acc. Chem. Res., 2008, 41, 1578-1586.
- 4 C. F. Bohren and D. R. Huffman, Absorption and Scattering of Light by Small Particles, Wiley-VCH Verlag GmbH, 1998.
- 5 J. N. Anker, W. P. Hall, O. Lyandres, N. C. Shah, J. Zhao and R. P. Van Duyne, Nat. Mater., 2008, 7, 442-453.
- 6 M. F. Kircher, A. de la Zerda, J. V. Jokerst, C. L. Zavaleta, P. J. Kempen, E. Mittra, K. Pitter, R. Huang, C. Campos, F. Habte, R. Sinclair, C. W. Brennan, I. K. Mellinghoff, E. C. Holland and S. S. Gambhir, Nat. Med., 2012, 18, 829-834.
- 7 M.-C. Daniel and D. Astruc, Chem. Rev., 2004, 104, 293-346.
- 8 O. Neumann, A. S. Urban, J. Day, S. Lal, P. Nordlander and N. J. Halas, ACS Nano, 2013, 7, 42-49.
- 9 J. Park, J.-H. Kang, X. Liu and M. L. Brongersma, Sci. Rep., 2015, 5, 15754.
- 10 P. B. Allen, Phys. Rev. Lett., 1987, 59, 1460-1463.
- 11 N. J. Hogan, A. S. Urban, C. Ayala-Orozco, A. Pimpinelli, P. Nordlander and N. J. Halas, Nano Lett., 2014, 14, 4640-4645.
- 12 T. W. Roberti, B. A. Smith and J. Z. Zhang, J. Chem. Phys., 1995, 102, 3860-3866.
- 13 F. Scotognella, G. Della Valle, A. R. Srimath Kandada, D. Dorfs, M. Zavelani-Rossi, M. Conforti, K. Miszta, A. Comin, K. Korobchevskaya, G. Lanzani, L. Manna and F. Tassone, Nano Lett., 2011, 11, 4711-4717.
- 14 D. B. Tice, S.-Q. Li, M. Tagliazucchi, D. B. Buchholz, E. A. Weiss and R. P. H. Chang, Nano Lett., 2014, 14, 1120-1126.

- 15 I. Kriegel, C. Urso, D. Viola, L. De Trizio, F. Scotognella, G. Cerullo and L. Manna, J. Phys. Chem. Lett., 2016, 7, 3873-3881.
- 16 B. T. Diroll, P. Guo, R. P. H. Chang and R. D. Schaller, ACS Nano, 2016, 10, 10099-10105.
- 17 M. Abb, Y. Wang, C. H. de Groot and O. L. Muskens, Nat. Commun., 2014, 5, 4869.
- 18 G. Della Valle, F. Scotognella, A. R. S. Kandada, M. Zavelani-Rossi, H. Li, M. Conforti, S. Longhi, L. Manna, G. Lanzani and F. Tassone, J. Phys. Chem. Lett., 2013, 4, 3337-3344.
- 19 M. Kanehara, H. Koike, T. Yoshinaga and T. Teranishi, J. Am. Chem. Soc., 2009, 131, 17736-17737.
- 20 D. J. Rowe, J. S. Jeong, K. A. Mkhoyan and U. R. Kortshagen, Nano Lett., 2013, 13, 1317-1322.
- 21 Y. Zhao, H. Pan, Y. Lou, X. Qiu, J. Zhu and C. Burda, J. Am. Chem. Soc., 2009, 131, 4253-4261.
- 22 T. Nütz, U.z. Felde and M. Haase, J. Chem. Phys., 1999, 110, 12142-12150.
- 23 J. M. Luther, P. K. Jain, T. Ewers and A. P. Alivisatos, Nat. Mater., 2011, 10, 361-366.
- 24 X. Pi and C. Delerue, *Phys. Rev. Lett.*, 2013, **111**, 177402.
- 25 S. D. Brorson, A. Kazeroonian, J. S. Moodera, D. W. Face, T. K. Cheng, E. P. Ippen, M. S. Dresselhaus and G. Dresselhaus, Phys. Rev. Lett., 1990, 64, 2172-2175.
- 26 J. Kim, G. K. Ong, Y. Wang, G. LeBlanc, T. E. Williams, T. M. Mattox, B. A. Helms and D. J. Milliron, Nano Lett., 2015, 15, 5574-5579.
- 27 S.-I. Choi, K. M. Nam, B. K. Park, W. S. Seo and J. T. Park, Chem. Mater., 2008, 20, 2609-2611.
- 28 R. J. Mendelsberg, G. Garcia, H. Li, L. Manna and D. J. Milliron, J. Phys. Chem. C, 2012, 116, 12226-12231.
- 29 K. Viswanathan, K. Brandt and E. Salje, J. Solid State Chem., 1981, 36, 45-51.
- 30 I. Hamberg and C. G. Granqvist, J. Appl. Phys., 1986, 60, R123-R160.
- 31 B. Willingham and S. Link, Opt. Express, 2011, 19, 6450-6461.
- 32 N. W. Ashcroft and N. D. Mermin, Solid State Physics, Brooks/Cole, Cengage Learning, 1976.
- 33 C. Sönnichsen, B. M. Reinhard, J. Liphardt and A. P. Alivisatos, Nat. Biotechnol., 2005, 23, 741-745.
- 34 J. Molenda and A. Kubik, *Phys. Status Solidi B*, 1995, **191**, 471.
- 35 J. H. Hodak, I. Martini and G. V. Hartland, J. Phys. Chem. B, 1998, 102, 6958-6967.
- 36 M. Adachi, Y. Akishige, T. Asahi, K. Deguchi, K. Gesi, K. Hasebe, T. Hikita, T. Ikeda, Y. Iwata, M. Komukae, T. Mitsui, E. Nakamura, N. Nakatani, M. Okuyama, T. Osaka, A. Sakai, E. Sawaguchi, Y. Shiozaki, T. Takenaka, K. Toyoda, T. Tsukamoto, T. Yagi, Y. Shiozaki, E. Nakamura and T. Mitsui, Oxides WO3, M2, Datasheet from Landolt-Börnstein - Group III Condensed Matter, 'Oxides' in Springer Materials, Springer-Verlag, Berlin Heidelberg, 2002, vol. 36A2, DOI: 10.1007/10857522_485.
- 37 B.-C. Kim, J.-H. Lee, J.-J. Kim and T. Ikegami, Mater. Lett., 2002, **52**, 114-119.
- 38 M. Perner, P. Bost, U. Lemmer, G. von Plessen, J. Feldmann, U. Becker, M. Mennig, M. Schmitt and H. Schmidt, Phys. Rev. Lett., 1997, 78, 2192-2195.